On the local corrosion behavior of coupled welded zones of the 2098-T351 Al-Cu-Li alloy produced by Friction Stir Welding (FSW): An amperometric and potentiometric microelectrochemical investigation

Rejane Maria P. da Silva [a,b,*], Javier Izquierdo [b,c], Mariana X. Milagre [a],
Abenchara Maria Betancor-Abreu [b], Leandro A. de Oliveira [d], Renato A. Antunes [d],
Ricardo M. Souto [b,c,**], Isolda Costa [a,***]

[a] *Instituto de Pesquisas Energéticas e Nucleares - IPEN/CNEN - Av. Prof. Lineu Prestes, 2242 São Paulo, Brazil*
[b] *Department of Chemistry, Universidad de La Laguna, P.O. Box 456, E-38200 La Laguna (Tenerife), Canary Islands, Spain*
[c] *Institute of Material Science and Nanotechnology, Universidad de La Laguna, P.O. Box 456, E-38200 La Laguna (Tenerife), Canary Islands, Spain*
[d] *Centro de Engenharia, Modelagem e Ciências Sociais Aplicadas (CECS), Universidade Federal do ABC (UFABC), Av. dos Estados 5001, 09210-580 Santo André, SP, Brazil*

ARTICLE INFO

ABSTRACT

Localized electrochemical methods supported by surface analytical characterizations were employed to investigate galvanic coupling effects and local electrochemical activity developed along the welded zones in Friction Stir Welded 2098-T351 Al-Cu-Li alloy. The investigation was carried out in the coupled weld joint/heat affected zones (WJ/HAZ) for both, the retreating (RS) and the advancing (AS) sides. The correlation between the surface chemistry, the microstructural characteristics and the electrochemical activity of these welded areas was studied. The results showed the development of galvanic interactions within and between the WJ and HAZ regions, which were imaged using the scanning vibrating electrode technique (SVET), and scanning electrochemical microscopy (SECM). SVET analyses showed that HAZ was more susceptible to the development of anodic sites than WJ. SECM in amperometric operation mode showed that WJ coupled to HAZ exhibited higher oxygen consumption and higher cathodic activity compared to HAZ. Furthermore, SECM in potentiometric operation showed alkalinization around WJ and increased acidity in HAZ, mainly at sites of severe localized corrosion (SLC). Based on the SVET and SECM results in combination with the surface analyses, it is proposed that the microgalvanic cells formed within these welded zones are due to the presence of secondary phases in the 2098-T351 alloy and their interactions with the adjacent matrix.

© 2021 Elsevier Ltd. All rights reserved.

1. Introduction

Al-Cu-Li alloys are under development for aerospace applications due to their higher specific strength than conventional Al-alloys. The addition of Li to these alloys reduces their density and increases their mechanical strength [1,2]. The weight reduction makes its application attractive in aircraft structures, thus reducing fuel consumption. However, Li additions also increase the susceptibility of Al-Cu alloys to localized corrosion reactions [3,4], a characteristic that is enhanced by welding. In fact, the welding processes are responsible for microstructural changes in the welded joint that result in macro-galvanic coupling and susceptibility to corrosion in different zones after welding [5–7].

Friction stir welding (FSW) has great potential as a welding process for aluminum alloys. This is a solid-state process that can be applied to difficult-to-weld materials, such as Al alloys, using conventional methods. This type of welding modifies the microstructure of the original material due to mechanical and thermal effects, leading to the formation of several zones with different microstructures [5,8]. Changes in microstructural characteristics due to the FSW process have been described in the literature [9–11]. The high temperatures reached and the intense plastic deformation of the weld joint (WJ) lead to the formation of a thermomechanically affected zone (TMAZ) and a stirring zone (SZ). In addition, thermal effects also differentiate the heat-affected zone (HAZ)

* Corresponding authors at: Instituto de Pesquisas Energéticas e Nucleares - IPEN/CNEN - Av. Prof. Lineu Prestes, 2242 São Paulo, Brazil.
** Corresponding authors at: Department of Chemistry, Universidad de La Laguna, P.O. Box 456, E-38200 La Laguna (Tenerife), Canary Islands, Spain.
E-mail addresses: rejanep2silva@gmail.com (R.M.P. da Silva), rsouto@ull.es (R.M. Souto), icosta@ipen.br (I. Costa).

from the unaffected parent metal (PM) [12–14]. Furthermore, due to differences in material flow and heat transfer on the two sides of the weld, the two sides of the joint have different microstructural characteristics [15–18]. Thus, on the retreating side (RS), the directions of the transverse motion and the tangential vector of the tool rotation speed are in opposite directions, while they are in the same direction for the advancing side (AS) [1–4]. Furthermore, material transport occurs from the RS side to AS [19].

Differences in the corrosion behavior of the RS and AS sides have been reported in the literature for various Alalloys [15–17], while changes in the welding parameters can produce additional effects on the corrosion behavior of the welded material [9]. When studying the FSW-welded Al 7020 alloy, Dudzik found that the RS was more susceptible to corrosion than AS [15], while Martins et al. [17] observed different electrochemical activities throughout the FSW-welded 2024-T3 Al alloy due to the uneven distribution and aggregation of coarse intermetallic particles in different zones of the welded joint. Clusters of coarse intermetallic particles were more evident in the TMAZ of the RS, increasing the susceptibility of this zone to localized corrosion. Recently, Milagre et al. [19] showed the influence of asymmetry effects arising from the FSW process on the susceptibility to localized corrosion of the 2098-T351 Al-Cu-Li alloy welded by FSW, and reported a higher electrochemical activity for RS compared to AS. The welding parameters used in that work [19] were different from those used in the current work. As previously indicated [9], the welding parameters can modify the extension, microstructure and, therefore, the corrosion activity of the weld zones [9]. The asymmetry observed in the work of Milagre et al. [19] was responsible for the differences in the electrochemical activity of the weld zones, in which the HAZ(RS) exhibited higher electrochemical activity compared to HAZ(AS). However, in the current work, it has been observed that dissimilarities in the local chemical composition of the welded surface contribute to differences in the electrochemical behavior of the weld zones.

The 2098 Al-Cu-Li alloy is a third generation Al-Li alloy [20] that was produced as a replacement for conventional 2XXX series aluminum alloys [21]. This alloy contains Cu, Li, Mg, Ag, Zr, Si, and Fe in its composition, which is responsible for its advanced microstructure and precipitation of hardening phases such as T1 (Al$_2$CuLi), which is described as the main reinforcement phase in the new generation of Al-Cu-Li alloys [22]. The T1 phase is reported to be very active due to the presence of Li, and its rapid selective dissolution leads to Cu-enrichment, polarity reversal, and then dissolution of the Al matrix in aggressive environments [1,3,23]. However, the quantity and morphology of this phase are modified by the FSW process [19], while causing different degrees of thermal gradients and mechanical deformations [5,8].

High corrosion activities have been reported for various FSW Al-Cu-Li alloys [5–8,24–27]. Among them, recent research by our group on the related AA2198 Al-Cu-Li alloy has shown that the parent material (PM) region is most susceptible to localized corrosion in FSW Al-Cu-Li alloys, a characteristic due to the greater amount of T1 phase that occurs in this region [6,7,27]. On the contrary, a greater resistance to localized corrosion has been observed in SZ, where the T1 phase is rare. Unfortunately, although it is accepted that Al-Cu-Li alloys are very sensitive to localized corrosion activity, there is controversy in the scientific literature about the localized distribution of corrosion processes throughout the FSW material [4,5,8,24,25]. For example, Corral et al. [24] have reported similar current densities and corrosion potentials for the FSW zone and the PM region of the 2195 Al alloy. Even rarer are the reports on the corrosion behavior of the 2098 Al-Cu-Li alloy [28–30].

Attempts have been made to study these localized processes using localized electrochemical techniques [19,31], although their ap-

plicability to study the corrosion activity of some Al-Cu-Li alloys has been shown in the literature [7,29,30,32]. Subsequently, the scanning vibrating electrode technique (SVET), scanning electrochemical microscopy (SECM), and local electrochemical impedance spectroscopy (LEIS) have been used successfully to study the effects of galvanic coupling between the different contacting regions developed for various Al alloys joined using FSW, specifically for the 7050/2024 [33], 2024/7475 [34], and 2050/7449 [35] systems. And more recently, differences in electrochemical reactivity resulting from the FSW treatment were observed using SECM when joining two samples of 2198-T851 Al-Cu-Li alloy, leading to the discovery that the most anodic zone was in the PM region, and this showed sites of severe localized corrosion (SLC) [27].

In this work, galvanic coupling effects and local electrochemical activity of the interfaces between welding zones interfaces in FSW 2098-T351 Al-Cu-Li alloy were investigated using a powerful combination of local electrochemical techniques. Electrochemical studies were carried out in the WJ/HAZ coupled welding zones (in both RS and AS cases) using potentiodynamic polarization in a micro-cell assembly, in combination with scanning electrochemical techniques (namely, SVET and SECM in amperometric and potentiometric operation modes). Although SECM in amperometric operation mode has already been used to characterize various Al-alloys [35–39], while potentiometric probes have proven to be interesting tools in the investigation of galvanic corrosion effects [40–43], the combined use of amperometric and potentiometric SECM probes to study different regions of Al-Cu-Li alloys welded by FSW has not been reported in literature. Thus, the novelty of this current work is the observation that through a detailed XPS study associated with potentiodynamic polarization in a micro-cell and the SVET technique, it was possible to show that the electrochemical activity of the coupled HAZ(RS)/WJ and HAZ(AS)/WJ regions, could be differentiated. The use of different SECM operation modes, with smaller scan areas and better resolution, was very important to observe and support the results obtained by other methods.

2. Experimental

2.1. Materials

Samples of a 2098-T351 alloy (3.4 wt% Cu, 1 wt% Li, 0.3 wt% Mg, 0.3 %wt Ag, 0.4 wt% Zr, 0.04 wt% Fe, 0.05 wt% Si, 0.02 wt% Zn, 0.003 wt% Mn) welded by friction stir welding (FSW) were used in this work. The FSW process was performed using a transverse speed of 150 mmmin^{-1} and a rotation rate of 1000 rpm. The diameter of the tool shoulder was 10 mm while that of the pin was 5 mm. All measurements were performed on the top surface of the FSW alloy. For that purpose, each sample was embedded in *Epofix* epoxy resin (Struers, Ballerup, Denmark) to produce a disk-shaped resin mount (dia. 3 cm), and cured for 24 h at ambient temperature. The top side of the mount with the sample at its center was abraded sequentially with #500, #800, #1500, #2500 and #4000 grit carbide silicon papers, and polished with diamond suspensions of 3 μm and 1 μm.

2.2. Microstructural and surface characterization

Optical microscopy was employed for surface observation after etching the surfaces in a solution with 2% (v/v) HF and 25% (v/v) HNO$_3$ in deionized water. Optical micrographs of the samples were also obtained after immersion in naturally-aerated 5 mmol L^{-1} NaCl solution for 24 h at room temperature (22 $\pm$ 2 °C). Vickers microhardness tests were carried out at the top surface of the FSW 2098-T351 alloy in successive steps of approximately 0.3 mm with a load of 0.3 g for 10 s of dwell time, using a HM-101 Mitutoyo Microhardness tester (Neuss, Germany).

The chemical composition of the surfaces was obtained by X-ray photoelectron spectroscopy (XPS) using a K-alpha$^+$ spectrometer (Thermo Fisher Scientific, Waltham, MS, USA). The beam was generated by a monochromatic Al K-α radiation source. The pressure in the analysis chamber was approximately 10^{-7} Pa. The spot size was 400 μm. The binding energy scale wascalibrated with respect to the C 1s peak (adventitious carbon) at 284.8 eV. High resolution spectra of the polished FSW 2098-T351 alloy were acquired before and after exposure to 5 mmol L^{-1} NaCl aqueous solution for 72 h.

2.3. Electrochemical characterization

Potentiodynamic polarization tests were specifically performed on different regions of the welded joint in the FSW 2098-T351 samples by using an electrochemical cell that limited approximately 0.20 cm^2 of the alloy. They were carried out using a Solartron 1287 potentiostat (Leicester, UK) in a conventional 3-electrode configuration, with a platinum wire as the auxiliary electrode, Ag/AgCl/KCl(sat) as reference electrode, and the FSW 2098-T351 sample as the working electrode. All potential values reported in this work are referred to the Ag/AgCl/KCl(sat) reference electrode. Polarization scans were carried out in naturally aerated 5 mmol L^{-1} NaCl solution at room temperature (22 $\pm$ 2 °C). The potential scans were recorded after 15 min exposure to the test solution in order to achieve a stable open circuit potential. They were initiated from a potential value 50 mV more negative than the corresponding OCP, and the potential was scanned in the positive direction up to +1.00 V with a scan rate of 0.5 mV s^{-1}. Experiments were performed in duplicate for the sake of reproducibility.

SVET measurements were performed using an Applicable Electronics instrument (New Haven, CT, USA) controlled by *Automated Scanning Electrode Technique* (ASET) software. A vibrating probe of Pt-Ir was used after platinization, in order to generate a spherical platinum black deposit of 20 μm diameter at the tip. The frequency of the probe vibration was 190 Hz along the *X* axis, and 70 Hz along the *Z* axis, both with an amplitude of 20 μm. Scans were carried out over the 2098-T351 welded samples (embedded in epoxy resin) at a height of approximately 170 μm, established using the in-built video-imaging system provided with the equipment. The SVET scans were carried out in naturally aerated 5 mmol L^{-1} NaCl solution at ambient temperature (22 $\pm$ 2 °C) for 3 h. The investigated sample was left unpolarized, effectively at its open circuit potential.

High-resolution Sensolytics SECM equipment (Bochum, Germany), built around an Autolab (Metrohm, Herisau, Switzerland) electrochemical interface and controlled with a personal computer, was used in two different operation modes: amperometric and potentiometric, by using Pt and Sb microelectrodes, respectively. The experiments were performed in aerated 5 mmol L^{-1} NaCl solution at room temperature (22 $\pm$ 2 °C) for 3 h. The sample was not polarized during the measurements.

For amperometric measurements, a platinum microdisk of 10 μm diameter was used. A Pt wire as counter electrode and a Ag/AgCl/KCl(sat) reference electrode completed the small electrochemical cell. The amperometric tests were performed using the redox competition mode with the Pt probe polarized at -0.70 V. This mode is related to the content of molecular oxygen dissolved in the test solution that is monitored from its electroreduction at the Pt probe. In this mode, the probe and the studied surface compete for the oxygen contained in the solution [44,45]. Scans were made in the *X-Y* plane with the Pt-probe located at a height of approximately 20 μm above the surface. To establish this working distance, a *Z*-approach curve was recorded above each region of the joint prior to measuring the corresponding SECM map. The redox competition mode was used and changes in the limiting cur-

rent for the electroreduction of dissolved oxygen were observed when the Pt probe approached the surface under investigation [44–46].

The potentiometric SECM measurements were carried out using an Sb microelectrode. For this, micropipettes were molded by pulling borosilicate capillaries (wall thickness 0.225 mm, outer diameter Ø = 1.5 mm) supplied by Hilgenberg GmbH (Malsfeld, Germany), using a model P-30 micropipette puller (Sutter Instrument, Novato, CA, USA). Subsequently, Cu wire (ca. 12 cm in length and 0.5 mm in diameter) and Sb fibre (2.0 cm in length and approximately 15-20 μm diameter) were used to fabricate the Sb microelectrode. The Sb fibre was inserted into the lumen of the micropipette with the tip protruding about 5 mm. The electrical contact of the Sb fibre and the Cu wire in the micropipette was obtained using a small quantity of liquid mercury metal. The two micropipette ends were sealed with *Loctite®* adhesive. More information on the manufacture of the Sb probe was given elsewhere [41]. In the measurement circuit, a voltage follower based on a 10^{13} input impedance operational amplifier (mod. TL071, Texas Instruments, Dallas, TX, USA) was inserted. The pH response of the Sb probe was then calibrated in a set of pH buffers. A linear relationship was obtained between the solution pH and the potential, with a slope of -44 mV per pH unit, in the 3 $\leq$ pH $\leq$ 11 range. Although the slope of the calibration line is less than the Nernstian slope, this is not unusual for these single barrel microelectrodes [47]. The Sb probe was then used in combination with an Ag/AgCl/KCl(sat) reference electrode for potentiometric SECM tests [45]. The Sb probe was placed at a height of approximately 50 μm above of the sample, adjusted using a video camera system.

3. Results and discussion

3.1. Surface characterization

The electrochemical characterization of the weld zones developed in FSW 2098-T351 alloy was designed to visualize their local electrochemical activities and reveal the impact of galvanic coupling between them due to variations in microstructure and composition. Local electrochemical behaviors must be characterized using spatially resolved electrochemical techniques rather than considering the average measurements provided by conventional electrochemical methods. Second, both the dimensions of the heterogeneous regions produced by the FSW procedure and the spatial resolution of the microelectrochemical methods must be taken into account to design the specific measurements to be performed and their relevance to describe the complete system. Surface analysis techniques were chosen for the identification and measurement of heterogeneous regions of the weld, as well as to characterize their chemical composition due to both the FSW treatment and the subsequent impact of corrosion. The metallographic characterization was carried out by measuring the microhardness profile in the weld, while XPS was used for the chemical characterization of the different regions identified by the first.

The metallographic characterization of FSW 2098-T351 showed the stir zone (SZ), the thermomechanically affected zone (TMAZ) and the heat affected zone (HAZ) (see Fig. 1a), although the dimensions of these zones are different from those observed in previous work [22] due to differences in the welding parameters and the tool geometry. The dimensions of the weld joint (WJ) were determined from the microhardness profile shown in Fig. 1b. That is, the WJ corresponds to the region of low microhardness values spanning approximately 10 mm and includes the TMAZ and SZ regions. The reduction in microhardness values observed in WJ is associated with the dissolution of the main reinforcement phase present in Al-Cu-Li alloys due to the high temperatures reached during the welding process [7,11,22].
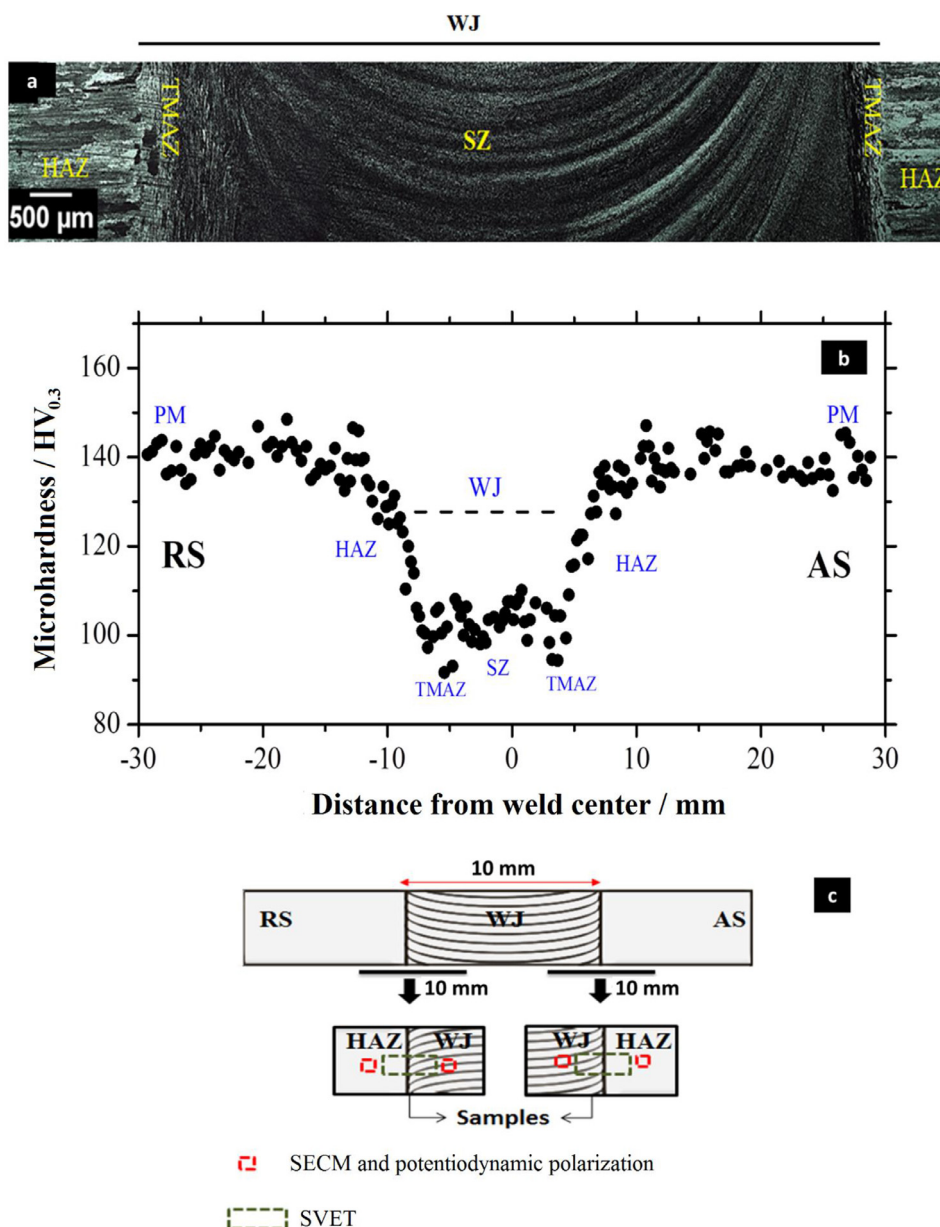
Fig. 1. Optical micrograph (a) and microhardness profile (b) of the top surface of the 2098-T351 Al-Cu-Li alloy welded by FSW showing the welding zones at the retreating side (RS) and advancing side (AS). (c) Sketch of the 2098-T351 welded by FSW showing the regions (red and green rectangles) actually sampled during the local electrochemical studies as indicated. (For interpretation of the references to color in this figure legend, the reader is referred to the web version of this article.)

To correlate the results of the local electrochemical behavior of the weld surfaces with changes in the local chemical composition of the material, an XPS analysis was performed. The WJ/HAZ(RS) and WJ/HAZ(AS) zones of FSW 2098-T351 were analyzed both for the pristine surface and for the surface resulting from the corrosion attack suffered during the exposure to 5 mmol L^{-1} NaCl aqueous solution for 72 h. Fig. 2 shows the high resolution spectra for Al2p, Cu2p and Li1s recorded in these weld areas, both before and after corrosion tests. Therefore, Fig. 2a-c show the spectra recorded for the WJ and HAZ(RS) zones in the polished and corroded conditions, while Fig. 2d-f depicts the spectra obtained for the WJ and HAZ(AS) zones under the same conditions. Two peaks for the Al2p signal were observed in Fig. 2a for the polished WJ/HAZ(RS) surface, one in the region of the lower binding energy region which is related to Al^0 (i.e., at 72.2 eV), while the other at the higher binding energy (75.4 eV) is related to the hydroxide/oxide layer that forms naturally on the surface of the material

[48,49]. In the polished condition, the Al2p signals were stronger for the HAZ(RS) region compared to WJ. The Al^0 signal was not detected in the HAZ(RS) zone after the corrosion test, while a very low intensity signal was observed for the element in the WJ region after corrosion, as shown in the Fig. 2a. Thus, the high resolution spectra (dotted curves) obtained on these surfaces show Al2p peaks around 74.0 and 74.5 eV, which are generally attributed to aluminum oxide/hydroxide [48]. After corrosion, the Al2p signals were slightly more intense for WJ than in the HAZ(RS) zone. On the other hand, Fig. 2d shows stronger Al2p signals in WJ than in WJ/HAZ(AS) for the polished condition. In addition, the two peaks of the Al2p signal described above can be found for the polished condition. In contrast, signals of very low intensity were observed for the Al^0 peak in the WJ and HAZ(AS) zones after the corrosion tests. The high resolution spectra (dotted curves) obtained for these corroded areas also showed Al2p peaks around 74.3 eV attributed to aluminum oxide/ hydroxide [48] (see Fig. 2d).
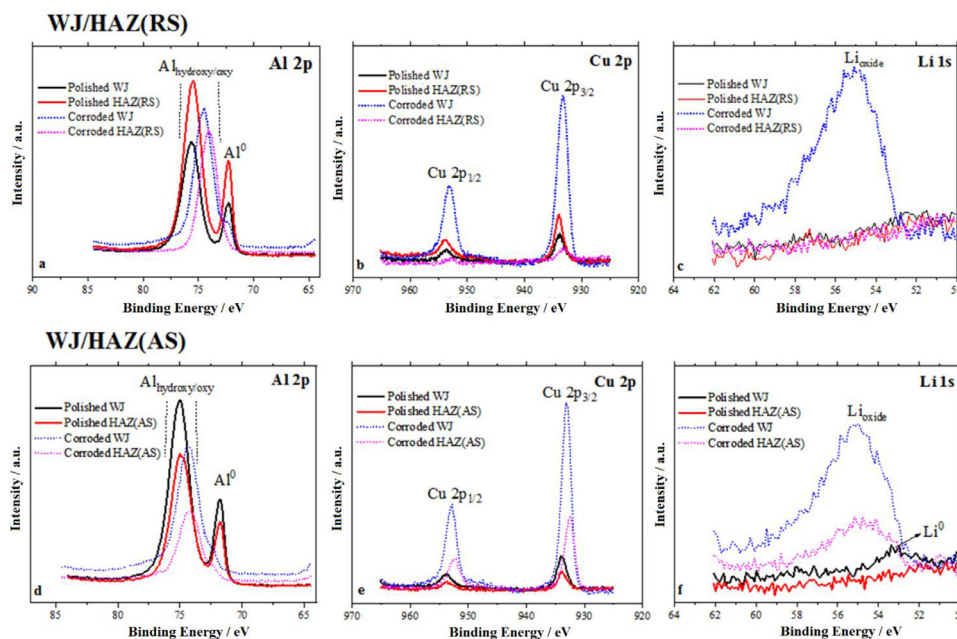
Fig. 2. High-resolution XPS spectra of Al, Cu and Li obtained in the welding zones of the 2098-T351 Al-Cu-Li alloy welded by FSW in the polished and corroded conditions. (a)-(c) spectra obtained in the WJ/HAZ of the retreating side (RS). (d)-(f) spectra obtained in the WJ/HAZ of the advancing side (AS).

Fig. 2b shows the high resolution spectra of Cu2p recorded in the WJ and HAZ(RS) zones. Binding energies of approximately 933.2 eV and 953.5 eV were observed for the polished and corroded welded areas. These peaks are linked to Cu [50,51], to the residual Cu-rich particles [52], and to the redeposition of Cu [53] in the alloy. After corrosion, the intensity of the Cu2p signal was considerably higher for WJ than for HAZ(RS) zones, indicating Cu enrichment in this region. The Cu2p signal was also stronger in WJ compared to HAZ(AS) after corrosion in Fig. 2e. During the welding process, the reached temperatures are high enough to cause the dissolution of phase T1 (Al_2CuLi) and, consequently, the diffusion of Cu towards the matrix. In addition, the movement of the tool in this process breaks the micrometric-sized particles and promotes their dispersion on the WJ surface [13], causing an increase in the specific surface corresponding to the Cu-enriched micrometric particles. Furthermore, the selective dissolution of the secondary phases can eventually lead to Cu dissolution, and it can re-precipitate in the cathodic regions, which would explain the stronger Cu2p signal in the WJ zone which is cathodic with respect to HAZ.

Li1s was not detected in the WJ/HAZ(RS) in the polished condition (see Fig. 2c). However, a Li1s peak was detected in the WJ region after the corrosion test, as shown by the blue dotted curve in Fig. 2c. This peak at approximately 55.1 eV is related to lithium oxide [54]. When the polished WJ/HAZ(AS) was analyzed, a low intensity peak at 53.0 eV related to Li^0 [54] was detected in WJ, but was not detected in HAZ (Fig. 2f). However, after corrosion, Li1s peaks around 55.1 eV were detected in both zones (WJ and HAZ(AS)), although they were stronger for WJ than for HAZ(AS), indicating that the thin oxide film of corrosion products, which was evenly distributed over the WJ, contains Li oxide. Changes in surface composition provide potential differences between WJ and HAZ. Therefore, differences in electrochemical activity and changes in pH should occur in these weldment zones, as will be discussed later.

The polished HAZ(RS) surface showed stronger Al2p and Cu2p signals compared to HAZ(AS) (see Fig. 3a-b). After corrosion, the Al2p signal was stronger in the case of HAZ(RS), although the Cu2p signal in this region was significantly weaker compared to

HAZ(AS). Li1s was only detected in the HAZ(AS) region after corrosion, as shown in Fig. 3c. Therefore, the corrosion product layer was enriched in Al and Cu in HAZ(RS), and enriched in Al, Cu and Li in HAZ(AS), as indicated by the spectra of the corroded surfaces compared to the polished conditions given in Fig. 3. The corrosion process was more intense in HAZ(AS) coupled to WJ and, therefore, greater intensities of Cu and Li signals were observed in this region. Due to the different microstructural characteristics of the HAZ on both sides of the weldment, changes in the corrosion behavior of these regions are likely to be observed.

3.2. Local electrochemical behavior of the weldment zones of the FSW 2098-T351 alloy

The width of the heterogeneous region produced by FSW has been found to extend to several millimeters as shown in the optical micrograph in Fig. 1a, while the effective spot sizes employed in scanning electrochemical microscopy (SECM) are generally 1 to 2 orders of magnitude smaller, whereas the scanning vibrating electrode technique (SVET) is typically employed to cover several hundred micrometers. Consequently, local microelectrochemical studies were designed to characterize the WJ/HAZ interface zones developed on both the advancing (AS) and the retreating sides (RS) when each of them was separately exposed to the test electrolyte as sketched in Fig. 1c. In this case, the galvanic coupling effects between the corresponding HAZ and WJ regions could be characterized because the samples contained portions of the two zones exposed simultaneously to the test solution. However, the different spatial resolutions of SVET and SECM required that the complete HAZ/WJ interface regions could only be imaged in one scan using SVET, whereas the higher spatial resolution of SECM motivated the imaging of smaller areas selected in HAZ and WJ zones. This was achieved by first imaging one of the zones, then moving the tip to the other side of the interface to image the other zone (see the small red-colored squares drawn in the sketch in Fig. 1c). On the other hand, an alternative procedure to using the scanning probe methods to achieve spatially resolved electrochemical results is to miniaturize the sample, effectively exposing to the electrolyte only the small area confined by a micro-cell. In
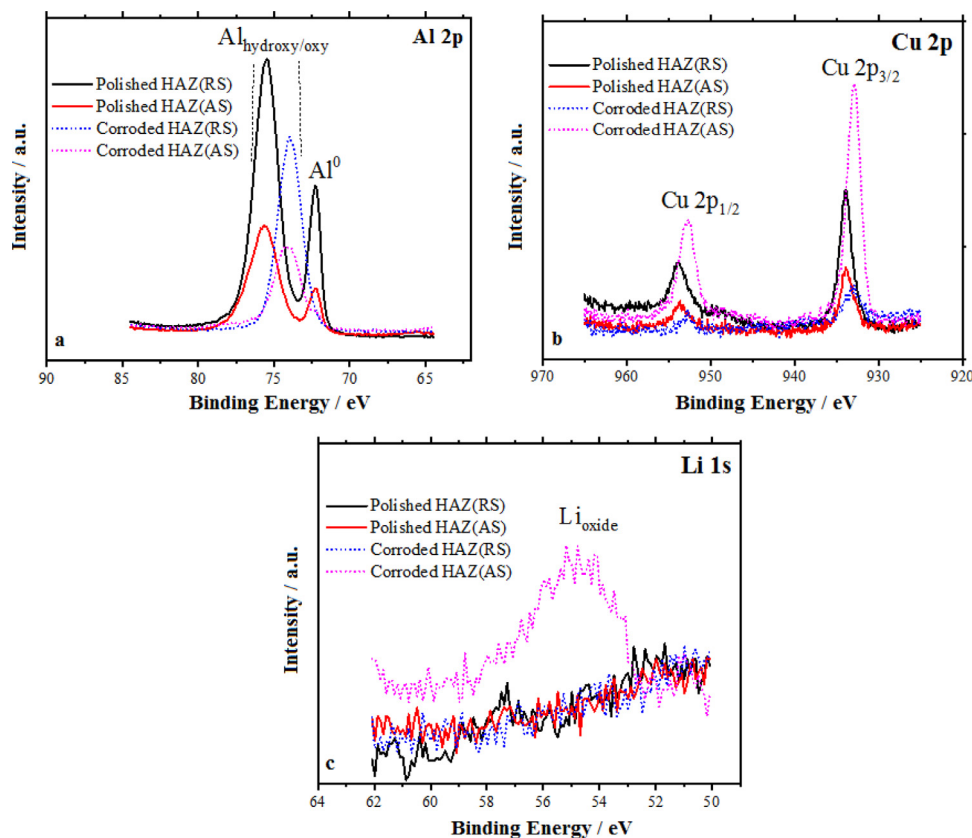
Fig. 3. High-resolution XPS spectra of (a) Al, (b) Cu and (c) Li obtained in the HAZ of the 2098-T351 Al-Cu-Li alloy welded by FSW in the polished and corroded conditions.

this way, the electrochemical response of the isolated region under study is obtained, because the other regions of the FSW are not exposed to the electrolyte, and therefore galvanic coupling effects do not effectively operate in that configuration (cf. Fig. 1c). In general, it is considered that the use of the three local electrochemical methods could provide complementary information for the characterization of the heterogeneous electrochemical activity of the WJ/HAZ(RS) and WJ/HAZ(AS) interfaces of the FSW alloy, as schematized in Fig. 1c.

3.2.1. Local potentiodynamic polarization (micro-cell)

Fig. 4 shows the anodic potentiodynamic polarization curves of the HAZ and WJ of the FSW 2098-T351 alloy obtained using an electrochemical micro-cell. As described above, this allows to evaluate the local electrochemical activity of specific zones in 5 mmol L^{-1} NaCl solution without any galvanic coupling between them or with any other region of the weldment. Specifically, in Fig. 4, the red curve shows the measured anodic polarization for a sample made up of HAZ(RS) and the black curve shows the corresponding anodic polarization curve of the HAZ(AS), both compared to WJ (blue curve). The potentiodynamic polarization curves measured for WJ in two separate samples as sketched in Fig. 1c, effectively indicated substantially the same electrochemical response as for the micro-cell configuration.

The anodic polarization curves are associated with the dissolution of the passive film. Thus, different electrochemical behaviors were observed in the different regions considered. From inspection of Fig. 4, it can be seen that WJ exhibits more noble potentials (with E_{corr} values around -0.30 V) compared to HAZ zones for the RS or AS sides, where E_{corr} values around -0.40 V were measured. Therefore, the possible differences between WJ and HAZ in both cases are around 100 mV. This potential difference explains the onset of a galvanic corrosion mechanism along the weldment. How-
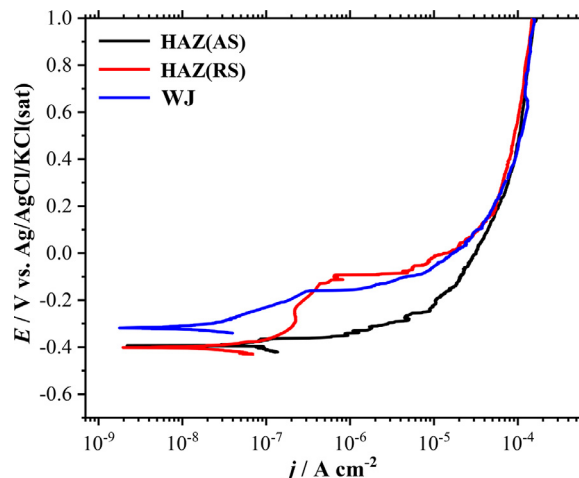

Fig. 4. Anodic potentiodynamic polarization curves of the HAZ and WJ regions of the 2098-T351 Al-Cu-Li alloy welded by FSW recorded in aerated 5 mmol L^{-1} NaCl solution. Scan rate: 0.5 mV s^{-1}.

ever, only on the basis of the polarization curves measured using a micro-cell, it was not possible to identify differences in the corrosion potentials of HAZ(RS) and HAZ(AS). Slightly lower current densities and pseudo-passive behavior are observed in the polarization curves measured in WJ. These results suggest that WJ is more corrosion resistant than HAZ in both RS and AS situations. The higher anodic current densities associated with faster dissolution are related to the curve measured for HAZ(AS) compared to that for HAZ(RS). However, HAZ(AS) and HAZ (RS) are more active than WJ.
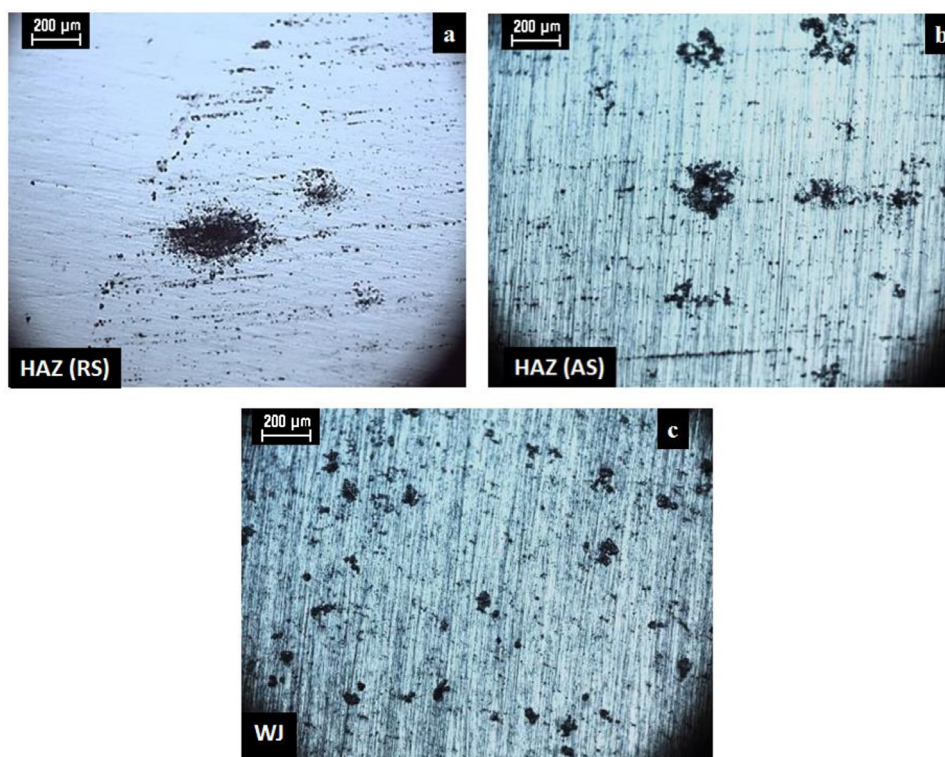
Fig. 5. Optical images of the weldment zones of the 2098-T351 Al-Cu-Li alloy welded by FSW after anodic potentiodynamic polarization.

After recording the polarization curves, the surfaces of the regions exposed to the test electrolyte were observed under an optical microscope as shown in Fig. 5. The WJ region was found to be more resistant to the appearance of SLC, although in the micrograph of Fig. 5c a non-severe but localized form of corrosion associated with attack around the micrometric particles was observed. In contrast, HAZ (from either RS or AS) exhibited SLC sites as shown in Fig. 5a-b. The anodic currents associated with SLC sites are significantly higher than those associated with micrometric particles. The contribution of SLC sites becomes significant in HAZ areas, contributing to the measurement of higher current densities compared to WJ. The differences in potential observed between the different zones of the weldment must be linked to the preferential dissolution of the T1 phase and to the enrichment of the matrix in Li and Cu produced during the FSW process, as confirmed by XPS characterization in Section 3.1. The Cu enrichment in WJ would increase the corrosion rate in the anodic regions of the weldment, while the smaller amounts of T1 phase in WJ would explain its significantly different electrochemical behavior compared to HAZ, and the appearance of galvanic coupling between WZ and HAZ (i.e., with a higher content of T1 phase). To study this effect, studies were carried out using scanning electrochemical techniques on these coupled weldment zones, as presented below.

3.2.2. Scanning vibrating electrode technique (SVET)

Fig. 6 shows the ionic current distributions recorded using the scanning vibrating electrode technique (SVET) for the coupled weldment zones submerged in aerated 5 mmol L^{-1} NaCl solution for 3 h. It should be noted that Fig. 6a-b show SVET maps obtained for WJ/HAZ(RS) and WJ/HAZ(AS) couplings, respectively. In both cases, corrosion activity was observed within 30 min of exposure to the test solution. In addition, the development of SLC sites was observed in the HAZ(RS) region of the weldment coupled to WJ in Fig. 6a. This shows that HAZ(RS) was more sensitive to the devel-

opment of SLC sites than WJ. Similar behavior was observed for the HAZ(AS) interface in Fig. 6b. The SVET results show that corrosion activities and ionic current densities were significantly higher in HAZ than in WJ. Therefore, on both sides of the weldment (i.e., AS and RS), WJ was more corrosion resistant according to the results presented in this work. The WJ was cathodic compared to the HAZ regions. These observations are in agreement with previous reports describing the development of galvanic coupling effects when WJ was coupled to adjacent regions in FSW Al-Cu-Li alloys [19,26,27]. That is, the WJ region became more resistant to corrosion when coupled with its adjacent zones, a characteristic directly related to the dissolution of the T1 phase in WJ. As a result, HAZ acts as an anode and is susceptible to severe localize corrosion (SLC), while WJ (with a lower density of T1 phase) acts as a cathode and SLC is not observed in this area.

In Fig. 6a, an anodic site was observed in the WJ with smaller ionic current densities compared to the anodic sites in the HAZ(RS). In contrast, no anodic sites were observed in the WJ of the coupled WJ/HAZ(AS) interface, showing a more efficient galvanic coupling effect between WJ and HAZ(AS) with the protection of the cathodic areas (WJ). In general, Fe-Cu-rich particles promote trenching [19,55], and the large quantity of these particles present in WJ increases the cathodic activity in this region. As a result, a microgalvanic coupling can occur between the Fe-Cu-rich particles and the adjacent matrix, thus promoting the formation of anodic sites in this region. It is known that the Li-rich phases are anodic with respect to the aluminum matrix [23,32], and a Li1s signal was detected in the WJ of the RS after corrosion (see Fig. 2c).

The SVET maps in Fig. 6a-b show that the highest anodic current densities were observed at the SLC sites. These are directly associated with the density of T1 phase, which is higher in HAZ (whether AS or RS) compared to WJ [22]. In WJ, the density of the T1 phase is very low according to the microhardness profile shown in Fig. 1b. Therefore, although anodic processes are associated with trenching, the ionic current densities related to this cor-
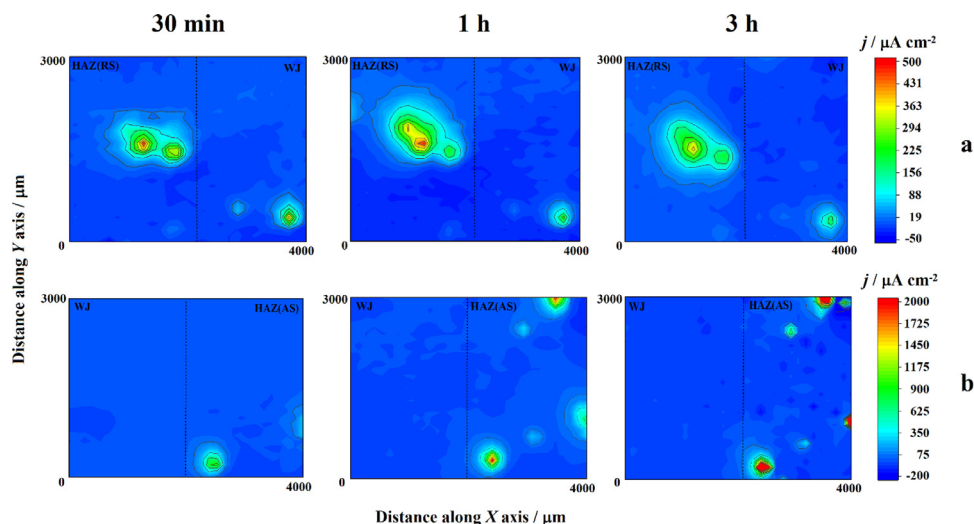
Fig. 6. SVET maps of the HAZ/WJ regions of the 2098-T351 Al-Cu-Li alloy welded by FSW recorded in aerated 5 mmol L^{-1} NaCl solution for different periods of immersion as indicated. (a) SVET maps obtained in the coupled weldment zones WJ/HAZ of the retreating side (RS), and (b) SVET maps obtained in the coupled weldment zones WJ/HAZ of the advancing side (AS).
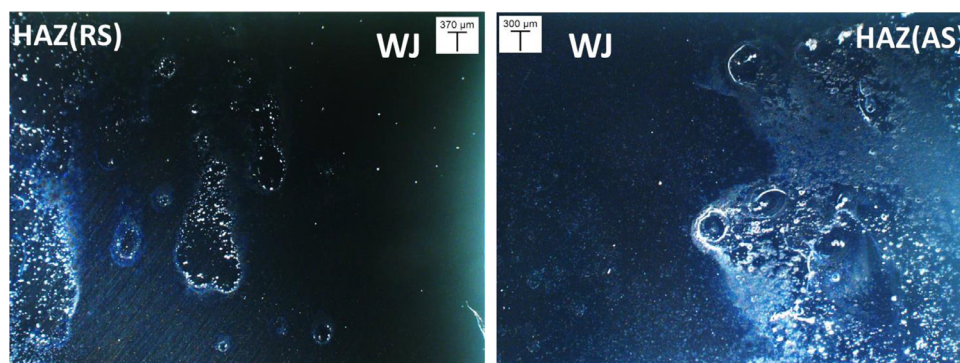

Fig. 7. Optical images of the coupled weldment zones of the FSW 2098-T351 Al-Cu-Li alloy retrieved after completing the SVET tests in Fig. 6.

rosion mechanism are quite low compared to those related to SLC activity.

The cathodic behavior in the WJ became apparent during immersion in the test solution, with a fairly uniform ionic current density distribution. The predominance of cathodic activity in WJ is due to the increase in the amount of micrometric particles in this region which results from the breakdown of the particles and the resulting drag caused by the movement of the tool in the FSW process [13]. As seen from the XPS results in Fig. 2a and 2e, the intensity of the Cu2p signal was considerably higher in WJ than in HAZ. The high intensity of Cu in this region is linked to micrometric particles enriched in Cu and/or to the redeposition of Cu at the cathodic sites. As mentioned above, the Cu-enrichment in WJ promotes corrosion activity in anodic areas, HAZ in the case of this study, either AS or RS.

The SVET maps given in Fig. 6 further showed that the anodic ionic current densities associated with the SLC sites were higher in the HAZ(AS) than in the HAZ(RS) when coupled to the WJ. A similar behavior was also observed in the anodic polarization curves shown in Fig. 4. Therefore, the extent of corrosion was different in the weldment zones due to galvanic coupling. After 3 h of immersion, the corrosion activity in the SLC regions (anodic sites) of the HAZ(AS) coupled to WJ had increased over time, and higher ionic current densities were detected above them relative to the same locations for shorter periods of immersion (see Fig. 6b). On the other hand, in the coupled WJ/HAZ(RS) interface, the corrosion activity at the anodic sites (SLC) decreased slightly with the

elapse of time according to Fig. 6a. The optical micrographs obtained in these areas after SVET test, shown in Fig. 7, corroborate these results, showing that the impact of corrosion was more intense in HAZ(AS) than in HAZ(RS), when coupled with WJ. However, different behaviors have been reported in previous works [15,17,19] for different Al alloys, in which the corrosion activity was more intense in RS than in AS. This effect must be associated with differences in the welding parameters, which produce different microstructural characteristics on the two sides of the weldment, which affects the corrosion activity on the welded material. In this current work, the XPS analysis showed differences in terms of the local surface chemical composition of the advancing side (AS) in relation to the retreating side (RS) (see Fig. 3). The higher Al2p peaks for HAZ(RS) suggest a more preserved naturally formed Al oxide (cf. Fig. 3a). Furthermore, the higher Cu2p signal observed for the HAZ(AS) after corrosion indicates a higher activity in HAZ(AS) (Fig. 3b), since it is known that the redeposition of Cu occurs near the anodic regions of the corroded 2xxx Al alloys. The results show the influence of the local surface chemical composition on the electrochemical activity of the welded 2098-T351 Al-Cu-Li alloy.

3.2.3. Scanning electrochemical microscopy (SECM)

First, amperometric scanning electrochemical microscopy (SECM) measurements were performed on the coupled WJ/HAZ(RS) and WJ/HAZ(AS) interfaces of the FSW 2098-T351 alloy, when immersed in aerated 5 mmol L^{-1} NaCl solution. For this, the
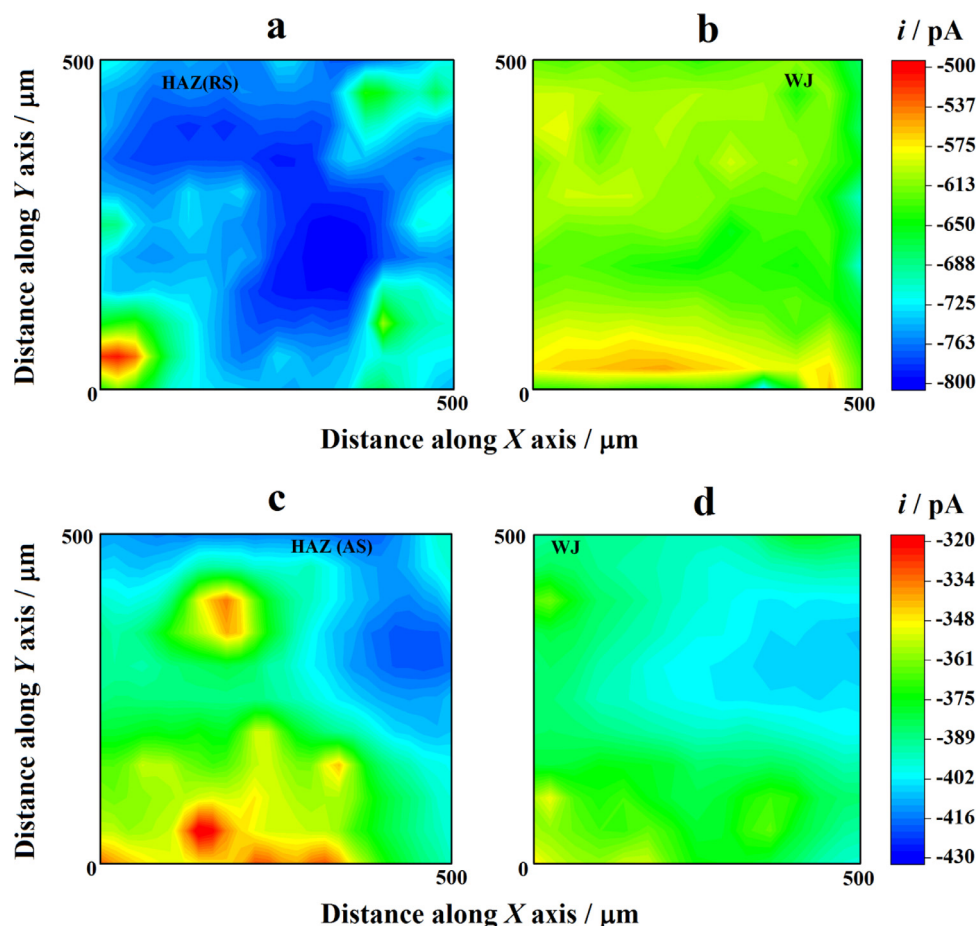
Fig. 8. Amperometric SECM maps obtained in the coupled weldment zones WJ/HAZ of the (a,b) retreating side (RS) and (c,d) advancing side (AS) of the 2098-T351 Al-Cu-Li alloy welded by FSW. They were recorded after approximately 3 h of immersion in aerated 5 mmol L^{-1} NaCl solution. Tip: Pt microelectrode biased at -0.70 V; tip-substrate distance: 20 μm; scan rate: 50 μm s^{-1}. (For interpretation of the references to color in this figure legend, the reader is referred to the web version of this article.)

amperometric Pt probe was used using the redox competition SECM mode. In this mode, there is redox competition for the electroreduction of dissolved oxygen in the aqueous solution between the cathodic regions developed in the corroding sample and the scanning probe [44]. As oxygen is consumed by both the probe and the surface under study, competition for this chemical species is established in the system [44–46]. The oxygen reduction reaction can be monitored by SECM under diffusion controlled conditions according to reaction (1) by setting the potential of the Pt probe to −0.70 V:

$$O_2 + 2H_2O + 4e^- \rightarrow 4OH^- \tag{1}$$

In Fig. 8, the SECM maps show the current distributions associated with oxygen depletion (i.e., oxygen consumption) between the coupled WJ and HAZ for the RS and AS situations. The SECM maps show the electrochemical responses related to oxygen electroreduction acquired at the coupled WJ/HAZ interfaces from locations taken from the samples as sketched in Fig. 1c. Therefore, the upper and lower color scales in Fig. 8 correspond to the different current intensities associated with oxygen consumption throughout the sample. In other words, the green/red/yellow colors represent regions with higher oxygen consumption by the surface, while the blue color scale indicates areas with lower oxygen depletion in the solution and therefore higher oxygen availability in the tip.

The measurement of the smallest oxygen reduction currents at the tip was expected to occur above the WJ as more oxygen would be consumed due to higher cathodic activity when coupled to HAZ (as shown by the SVET maps in Fig. 6). As a result, oxygen reduc-

tion takes place at the WJ surface. In fact, the SECM maps given in Fig. 8a-b show that the highest oxygen reduction currents were measured at the tip when scanning over the HAZ(RS) than in WJ (see the largest blue region), because this region exhibited a more anodic behavior. Therefore, this observed difference occurs due to macro-coupling between WJ and HAZ(RS). A closer inspection of Fig. 8 reveals discrete locations that have higher oxygen consumption within the HAZ(RS) region (green/red colors). As described above, microgalvanic coupling can also occur between the Fe-Cu-enriched particles and the adjacent matrix. Interestingly, Araujo et al. [56] described several localized corrosion mechanisms associated with 2198 Al-Cu-Li alloy in different temper conditions. They reported that anodic reactions in the matrix around the micrometric particles cause Cu enrichment depending on the preferential dissolution of Al and Li and, therefore, oxygen reduction occurs in the cathodic particles. Next, a potential difference between the matrix and the constituent particles was shown using the Volta potential maps of the constituent particles in the Al-Cu-Li alloy matrix that were obtained by SKPFM [56]. That is, higher potentials were recorded for the constituent particles compared to the matrix, and the authors suggested that galvanic coupling between the constituent particles and the matrix may occur as the origin of the localized attack.

The SECM maps of HAZ and WJ in the case of the AS of the weldment were measured in the same way and are depicted in Fig. 8c-d. It can be seen that HAZ(AS) exhibited larger areas of oxygen consumption at the surface (i.e., red, yellow and green color regions) compared to HAZ(RS) (see Fig. 8a). In accordance with the
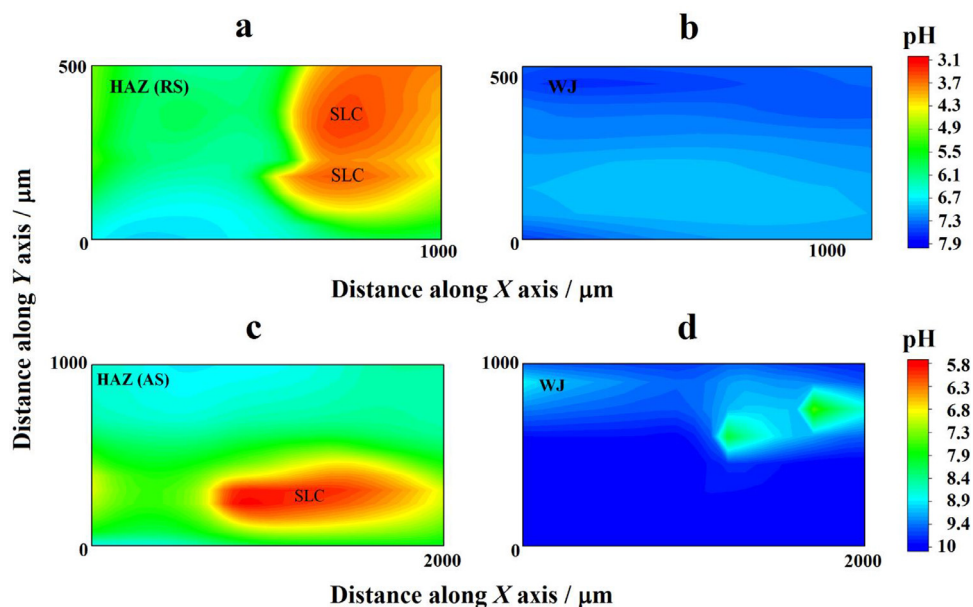
Fig. 9. Potentiometric SECM maps obtained in the coupled weldment zones WJ/HAZ of (a,b) the retreating side (RS) and (c,d) advancing side (AS) of the 2098-T351 Al-Cu-Li alloy welded by FSW after approximately 3 h of immersion in aerated 5 mmol L^{-1} NaCl solution. Tip: Sb microelectrode; tip-substrate distance: 50 μm; scan rate: 80 μm s^{-1}. (For interpretation of the references to color in this figure legend, the reader is referred to the web version of this article.)

results obtained using the other localized electrochemical methods above, the electrochemical activity of HAZ(AS) was higher compared to HAZ(RS). Since the high temperatures reached on this side of the weldment favor a greater dissolution of the T1 phase [22], the more active elements of the T1 phase (Al and Li) dissolve preferentially and, consequently, Cu is enriched in this region and it works as efficient cathodes for oxygen reduction. However, despite this localized behavior, in general, when considering the full galvanic macro-coupling between HAZ(AS), HAZ(RS) and WJ, the latter will act preferentially as the cathode (i.e., higher oxygen consumption by the surface), and the HAZ on both sides will function as an anode (higher oxygen availability at the tip).

Second, potentiometric SECM operation using a Sb/Sb$_2$O$_3$ tip allowed imaging spatially-resolved pH distributions occurring around the same interfaces formed by the coupled welded zones during immersion in naturally-aerated 5 mmol L^{-1} NaCl solution, and are shown in Fig. 9. In aerated solutions at neutral or alkaline pH, the reduction of oxygen is the main cathodic process, according to reaction (1). As can be seen, oxygen reduction leads to local alkalinization in the cathodic regions. On the other hand, at the anodic sites, the main reactions are related to metal dissolution, as indicated:

$$Al \rightarrow Al^{3+} + 3e^- \tag{2}$$

In Fig. 9, the blue/green color scale corresponds to regions with higher pH, while the red scale color corresponds to the sites with lower pH. Local acidification was observed above HAZ, primarily associated with the regions that develop SLC sites, while alkalinization occurred above the corroding WJ. As the SVET maps in Fig. 6 show, the highest anodic currents were observed at the SLC sites present in the HAZ. In the corrosion process, the oxidation of Al to Al^{3+} (according to reaction (2)) occurs in the anodic regions. In addition, hydrogen is released due to hydrolysis of dissolved metal ions; therefore, a significant decrease in pH occurs inside the corroding pit, leading to the observation of local acidification in the electrolyte adjacent to the SLC regions. The corrosion process at these sites is autocatalytic, favoring the continuous generation of H$^+$. On the other hand, in the WJ, it was observed that

this region is not susceptible to the development of SLC sites and that the attack in this zone is mainly associated with the presence of micrometric particles (cf. Fig. 5c). These cathodic particles uniformly distributed in the WJ region, in addition to the dissolution of the T1 phase, explain the high cathodic activity observed in this region. As a result, higher pH values were observed in this zone. On the other hand, the lower pH regions observed in Fig. 9 are directly associated with the SLC process. They were clearly observable in both HAZ regions (either from the AS or RS) coupled to WJ, while the latter presented higher and more uniform pH distributions for the two coupled interfaces, therefore directly related to the high cathodic activity concentrated in this region. This behavior is in agreement with the observations obtained with the other experimental methods used in this work.

4. Conclusions

The distribution of electrochemical behavior developed in the coupled weldment zones (namely, the weld joint (WJ) and the heat affected zone (HAZ)), either on the advancing (AS) or the retreating (RS) sides, of the FSW 2098-T351 Al-Cu-Li alloy was investigated when exposed to a dilute aqueous solution containing chloride ions. Macro-galvanic interactions between the coupled WJ/HAZ interfaces and micro-galvanic interactions within these zones have been observed using a powerful combination of localized electrochemical methods. Analysis of the anodic potentiodynamic polarization curves in a micro-cell and the SVET maps showed that the HAZ, whether in AS or RS, behaved anodic to WJ, and was more susceptible to the development of severe localized corrosion (SLC) sites compared to WJ. In fact, the WJ was more resistant to localized corrosion than HAZ. Furthermore, these techniques showed that the electrochemical activity of HAZ(AS) coupled to WJ was higher than that of HAZ(RS), which was related to differences in the local surface chemical composition obtained by X-ray photoelectron spectroscopy (XPS). On the other hand, scanning electrochemical microscopy (SECM), operated in amperometric and potentiometric modes, was useful to monitor oxygen consumption related to cathodic activity and pH distribution along the coupled welded zones, respectively. The SECM results showed

that higher cathodic activities and, consequently, higher alkalinization were observed in WJ, which was correlated with a lower content of T1 phase, compared to HAZ (either in AS or in RS). SECM in the potentiometric mode also showed that intense acidification occurred at the SLC sites in the HAZ. Therefore, localized amperometric and potentiometric techniques have proven very useful in providing a new understanding of the effects of galvanic coupling and local electrochemical activity of interfaces in welded zones of Al-Cu-Li alloys produced by FSW.

Declaration of Competing Interest

The authors declare that they have no known competing financial interests or personal relationships that could have appeared to influence the work reported in this paper.

Credit authorship contribution statement

Rejane Maria P. da Silva: Conceptualization, Investigation, Data curation, Validation, Visualization, Writing - original draft, Writing - review & editing. **Javier Izquierdo:** Data curation, Supervision, Visualization, Methodology, Writing - review & editing. **Mariana X. Milagre:** Investigation, Writing - review & editing. **Abenchara Maria Betancor-Abreu:** Investigation. **Leandro A. de Oliveira:** Investigation. **Renato A. Antunes:** Investigation. **Ricardo M. Souto:** Data curation, Supervision, Methodology, Funding acquisition, Writing - original draft, Writing - review & editing. **Isolda Costa:** Supervision, Resources, Funding acquisition, Writing - review & editing.

Acknowledgements

References

[1] R.G. Buchheit, J.P. Moran, G.E. Stoner, Electrochemical behavior of the T1 (Al2CuLi) intermetallic compound and its role in localized corrosion of Al-2% Li-3% Cu alloys, Corrosion 50 (1994) 120–130, doi:10.5006/1.3293500.

[2] R.J. Rioja, J. Liu, The evolution of Al-Li base products for aerospace and space applications, Metall. Mater. Trans. A 43 (2012) 3325–3337, doi:10.1007/s11661-012-115.

[3] R.G. Buchheit, J.P. Moran, G.E. Stoner, Localized corrosion behavior of alloy 2090—The role of microstructural heterogeneity, Corrosion 46 (1990) 610–617, doi:10.5006/1.3585156.

[4] V. Proton, J. Alexis, E. Andrieu, J. Delfosse, A. Deschamps, F. De Geuser, M.C. Lafont, C. Blanc, The influence of artificial ageing on the corrosion behaviour of a 2050 aluminium-copper-lithium alloy, Corros. Sci. 80 (2014) 494–502, doi:10.1016/j.corsci.2013.11.060.

[5] X. Zhang, B. Liu, X. Zhou, J. Wang, C. Luo, Z. Sun, Z. Tang, F. Lu, Corrosion behavior of friction stir welded 2A97 Al-Cu-Li alloy, Corrosion 73 (2017) 988–997, doi:10.5006/2418.

[6] U. Donatus, R.O. Ferreira, N.V.V. Mogili, B.V.G. de Viveiros, M.X. Milagre, I. Costa, Corrosion and anodizing behaviour of friction stir weldment of AA2198-T851 Al-Cu-Li alloy, Mater. Chem. Phys. 219 (2018) 493–511, doi:10.1016/j.matchemphys.2018.08.053.

[7] U. Donatus, B.V.G. de Viveiros, M.C. de Alencar, R.O. Ferreira, M.X. Milagre, I. Costa, Correlation between corrosion resistance, anodic hydrogen evolution and microhardness in friction stir weldment of AA2198 alloy, Mater. Charact. 144 (2018) 99–112, doi:10.1016/j.matchar.2018.07.004.

[8] V. Proton, J. Alexis, E. Andrieu, C. Blanc, J. Delfosse, L. Lacroix, Influence of postwelding heat treatment on the corrosion behavior of a 2050-T3 aluminumcopper-lithium alloy friction stir welding joint, J. Electrochem. Soc. 158 (2011) C139–C147, doi:10.1149/1.3562206.

[9] M. Jariyaboon, A.J. Davenport, R. Ambat, B.J. Connolly, S.W. Williams, D.A. Price, The effect of welding parameters on the corrosion behaviour of friction stir

[10] J.C. Rao, E.J. Payton, C. Somsen, K. Neuking, G. Eggeler, A. Kostka, J.F. Dos Santos, Where does the lithium go? - A study of the precipitates in the stir zone of a friction stir weld in a li-containing 2xxx series Al alloy, Adv. Eng. Mater. 12 (2010) 298–303, doi:10.1002/adem.200900284.

[11] W. Li, R. Jiang, Z. Zhang, Y. Ma, Effect of rotation speed to welding speed ratio on microstructure and mechanical behavior of friction stir welded aluminiumlithium alloy joints, Adv. Eng. Mater. 15 (2013) 1051–1058, doi:10.1002/adem.201300147.

[12] R.W. Fonda, J.F. Bingert, Precipitation and grain refinement in a 2195 Al friction stir weld, Metall. Mater. Trans. A 37 (2006) 3593–3604, doi:10.1007/s11661-006-1054-2.

[13] R. Nandan, T. Debroy, H.K.D.H. Bhadeshia, Recent advances in friction stir welding – Process, weldment structure and properties, Prog. Mater Sci. 53 (2008) 980–1023, doi:10.1016/j.pmatsci.2008.05.001.

[14] P.L. Threadgill, A.J. Leonard, H.R. Shercliff, P.J. Withers, Friction stir welding of aluminium alloys, Int. Mater. Rev. 54 (2009) 49–93, doi:10.1179/174328009X411136.

[15] K. Dudzik, Properties of advancing side of weld in joint welded by FSW, J. KONES Powertrain Transp. 21 (2014) 75–80, doi:10.5604/12314005.1133167.

[16] Y. Deng, B. Peng, G. Xu, Q. Pan, Z. Yin, Stress corrosion cracking of a highstrength friction-stir-welded joint of an Al−Zn−Mg−Zr alloy containing 0.25 wt.% Sc, Corros. Sci. 100 (2015) 52–72, doi:10.1016/j.corsci.2015.06.031.

[17] F. Martins, U. Donatus, O. Maurício, P. Ramirez, G. De Viveiros, S. Lamaka, M. Zheludkevich, M. Masoumi, V. Vivier, I. Costa, H. Gomes, D. Melo, Effect of unequal levels of deformation and fragmentation on the electrochemical response of friction stir welded AA2024-T3 alloy, Electrochim. Acta 313 (2019) 271–281, doi:10.1016/j.electacta.2019.04.137.

[18] R.S. Mishra, Z.Y. Ma, Friction stir welding and processing, Mater. Sci. Eng. R: Rep. 50 (2005) 1–78, doi:10.1016/j.mser.2005.07.001.

[19] M.X. Milagre, U. Donatus, N.V. Mogili, R.M.P. Silva, B.V.G. de Viveiros, V.F. Pereira, R.A. Antunes, C.S.C. Machado, J.V.S. Araujo, I. Costa, Galvanic and asymmetry effects on the local electrochemical behavior of the 2098-T351 alloy welded by friction stir welding, J. Mater. Sci. Technol. 45 (2020) 162–175, doi:10.1016/j.jmst.2019.11.016.

[20] T. Warner, Recently-developed aluminium solutions for aerospace applications, Mater. Sci. Forum 519–521 (2006) 1271–1278 10.4028/, www.scientific.net/MSF.519-521.1271 .

[21] H.G. Salem, J.S. Lyons, Effect of equal channel angular extrusion on the microstructure and superplasticity of an Al-Li alloy, J. Mater. Eng. Perform. 11 (2002) 384–391, doi:10.1361/105994902770343908.

[22] M.X. Milagre, N.V. Mogili, U. Donatus, R.A.R. Giorjão, M. Terada, J.V.S. Araujo, C.S.C. Machado, I. Costa, On the microstructure characterization of the AA2098-T351 alloy welded by FSW, Mater. Charact. 140 (2018) 233–246, doi:10.1016/j.matchar.2018.04.015.

[23] J.F. Li, C.X. Li, Z.W. Peng, W.J. Chen, Z.Q. Zheng, Corrosion mechanism associated with T1 and T2 precipitates of Al-Cu-Li alloys in NaCl solution, J. Alloys Compd. 460 (2008) 688–693, doi:10.1016/j.jallcom.2007.06.072.

[24] J. Corral, E.A. Trillo, Y. Li, L.E. Murr, Corrosion of friction-stir welded aluminum alloys 2024 and 2195, J. Mater. Sci. Lett. 19 (2000) 2117–2122, doi:10.1023/A:1026710422951.

[25] V. Proton, J. Alexis, E. Andrieu, J. Delfosse, M.C. Lafont, C. Blanc, Characterisation and understanding of the corrosion behaviour of the nugget in a 2050 aluminium alloy Friction Stir Welding joint, Corros. Sci. 73 (2013) 130–142, doi:10.1016/j.corsci.2013.04.001.

[26] C. Machado, U. Donatus, M. Xavier Milagre, N. Mogili, R. Giorjão, R. Klumpp, J.V. Araujo, R. Ferreira, I. Costa, Correlating the modes of corrosion with microstructure in friction stir welded AA2198-T8 alloy in aqueous hydrogen peroxide-chloride medium, Corrosion 75 (2019) 628–640, doi:10.5006/3054.

[27] U. Donatus, R.M.P. da Silva, J.V.S. Araujo, M.X. Milagre, C.P. de Abreu, C.S.C. Machado, I. Costa, Macro and microgalvanic interactions in friction stir weldment of AA2198-T851 alloy, J. Mater. Res. Technol. 8 (2019) 6209–6222, doi:10.1016/j.jmrt.2019.10.015.

[28] E. Ghanbari, A. Saatchi, X. Lei, D. Kovalov, D.D. Macdonald, Passivity breakdown and pitting corrosion of Al-Li aerospace alloys, in: Proceedings of the Department of Defense (DoD) - Allied Nations Technical Corrosion Conference, 2017, pp. 1–15.

[29] M.X. Milagre, U. Donatus, C.S.C. Machado, J.V.S. Araujo, R.M.P. da Silva, B.V.G. de Viveiros, A. Astarita, I. Costa, Comparison of the corrosion resistance of an Al–Cu alloy and an Al–Cu–Li alloy, Corrosion Engineering, Sci. Technol. 54 (2019) 402–412, doi:10.1080/1478422X.2019.1605472.

[30] R.M.P. da Silva, M.X. Milagre, L.A. de Oliveira, U. Donatus, R.A. Antunes, I. Costa, The local electrochemical behavior of the AA2098-T351 and surface preparation effects investigated by scanning electrochemical microscopy, Surf. Interface Anal. 51 (2019) 982–992, doi:10.1002/sia.6682.

[31] M.X. Milagre, U. Donatus, C.S.C. Machado, J. Victor, S. Araujo, R.O. Ferreira, R. Maria, P. Silva, R.A. Antunes, Exfoliation corrosion susceptibility in the zones of friction stir welded AA2098-T351, J. Mater. Res. Technol. 8 (2019) 1–14, doi:10.1016/j.jmrt.2019.09.066.

[32] J.V.S. Araujo, U. Donatus, F.M. Queiroz, M. Terada, M.X. Milagre, M.C. de Alencar, I. Costa, On the severe localized corrosion susceptibility of an AA2198-T851 alloy, Corros. Sci. 133 (2018) 132–140, doi:10.1016/j.corsci.2018.01.028.

[33] J.C.B. Bertoncello, S.M. Manhabosco, L.F.P. Dick, Corrosion study of the friction stir lap joint of AA7050-T76511 on AA2024-T3 using the scanning vibrating electrode technique, Corros. Sci. 94 (2015) 359–367, doi:10.1016/j.corsci.2015.02.029.

[34] C.P. de Abreu, I. Costa, H.G. de Melo, N. Pébère, B. Tribollet, V. Vivier, Multiscale electrochemical study of welded Al alloys joined by friction stir welding, J. Electrochem. Soc. 164 (2017) C735–C746, doi:10.1149/2.0391713jes.

[35] D. Sidane, E. Bousquet, O. Devos, M. Puiggali, M. Touzet, V. Vivier, Local electrochemical study of friction stir welded aluminum alloy assembly, J. Electroanal. Chem. 737 (2014) 206–211, doi:10.1016/j.jelechem.2014.06.025.

[36] J.C. Seegmiller, D.A. Buttry, A SECM study of heterogeneous redox activity at AA2024 surfaces, J. Electrochem. Soc. 150 (2003) B413–B418, doi:10.1149/1.1593041.

[37] M.B. Jensen, A. Guerard, D.E. Tallman, G.P. Bierwagen, Studies of electron transfer at aluminum alloy surfaces by scanning electrochemical microscopy, J. Electrochem. Soc. 155 (2008) C324–C332, doi:10.1149/1.2916734.

[38] H. Zhou, X. Li, C. Dong, K. Xiao, T. Li, Corrosion behavior of aluminum alloys in Na$_2$SO$_4$ solution using the scanning electrochemical microscopy technique, Int. J. Miner. Metall. Mater. 16 (2009) 84–88, doi:10.1016/S1674-4799(09)60014-5.

[39] D.J. Carbonell, A. García-Casas, J. Izquierdo, R.M. Souto, J.C. Galván, A. Jiménez-Morales, Scanning electrochemical microscopy characterization of sol-gel coatings applied on AA2024-T3 substrate for corrosion protection, Corros. Sci. 111 (2016) 625–636, doi:10.1016/j.corsci.2016.06.002.

[40] E. Tada, S. Satoh, H. Kaneko, The spatial distribution of Zn^{2+} during galvanic corrosion of a Zn/steel couple, Electrochim. Acta 49 (2004) 2279–2285, doi:10.1016/j.electacta.2004.01.008.

[41] J. Izquierdo, L. Nagy, Á. Varga, J.J. Santana, G. Nagy, R.M. Souto, Spatially resolved measurement of electrochemical activity and pH distributions in corrosion processes by scanning electrochemical microscopy using antimony microelectrode tips, Electrochim. Acta 56 (2011) 8846–8850, doi:10.1016/j.electacta.2011.07.076.

[42] Volumen 2 R.M. Souto, J. Izquierdo, J.J. Santana, A. Kiss, L. Nagy, G. Nagy, Progress in scanning electrochemical microscopy by coupling potentiometric and amperometric measurement modes, in: A. Méndez-Vilas (Ed.), Current Microscopy Contributions to Advances in Science and Technology, Formatex Research Center, Badajoz (Spain), 2012, pp. 1407–1415. Volumen 2.

[43] V.A. Nazarov, M.G. Taryba, E.A. Zdrachek, K.A. Andronchyk, V.V. Egorov, S.V. Lamaka, Sodium- and chloride-selective microelectrodes optimized for corrosion studies, J. Electroanal. Chem. 706 (2013) 13–24, doi:10.1016/j.jelechem.2013.07.034.

[44] A.C. Bastos, A.M. Simões, S. González, Y. González-García, R.M. Souto, Imaging concentration profiles of redox-active species in open-circuit corrosion processes with the scanning electrochemical microscope, Electrochem. Commun. 6 (2004) 1212–1215, doi:10.1016/j.elecom.2004.09.022.

[45] R.M.P. da Silva, J. Izquierdo, M.X. Milagre, A.M. Betancor-Abreu, I. Costa, R.M. Souto, Use of amperometric and potentiometric probes in scanning elec-

trochemical microscopy for the spatially-resolved monitoring of severe localized corrosion sites on aluminum alloy 2098-T351, Sensors 21 (2021) 1132, doi:10.3390/s21041132.

[46] R.M. Souto, L. Fernández-Mérida, S. González, SECM imaging of interfacial processes in defective organic coatings applied on metallic substrates using oxygen as redox mediator, Electroanalysis 21 (2009) 2640–2646, doi:10.1002/elan.200900232.

[47] B.M. Fernández-Pérez, J. Izquierdo, S. González, R.M. Souto, Scanning electrochemical microscopy studies for the characterization of localized corrosion reactions at cut edges of coil-coated steel, J. Solid State Electrochem. 18 (2014) 2983–2992, doi:10.1007/s10008-014-2397-z.

[48] A. Uhart, J.C. Dupin, J.P. Bonino, D. Gonbeau, J. Esteban, J.B. Ledeuil, F. Ansart, An Auger and XPS survey of cerium active corrosion protection for AA2024-T3 aluminum alloy, Appl. Surf. Sci. 390 (2016) 751–759, doi:10.1016/j.apsusc.2016.08.170.

[49] L. Jinlong, L. Hongyun, L. Tongxiang, Investigation of microstructure and corrosion behavior of burnished aluminum alloy by TEM, EWF, XPS and EIS techniques, Mater. Res. Bull. 83 (2016) 148–154, doi:10.1016/j.materresbull.2016.05.013.

[50] P. Campestrini, H. Terryn, A. Hovestad, J.H.W. de Wit, Formation of a cerium-based conversion coating on AA2024: relationship with the microstructure, Surf. Coat. Technol. 176 (2004) 365–381, doi:10.1016/S0257-8972(03)00743-6.

[51] R. Grilli, M.A. Baker, J.E. Castle, B. Dunn, J.F. Watts, Localized corrosion of a 2219 aluminium alloy exposed to a 3.5% NaCl solution, Corros. Sci. 52 (2010) 2855–2866, doi:10.1016/j.corsci.2010.04.035.

[52] S.A. Kulinich, A.S. Akhtar, P.C. Wong, K.C. Wong, K.A.R. Mitchell, Growth of permanganate conversion coating on 2024-Al alloy, Thin Solid Films 515 (2007) 8386–8392, doi:10.1016/j.tsf.2007.04.164.

[53] R. Viroulaud, J. Światowska, A. Seyeux, S. Zanna, J. Tardelli, P. Marcus, Influence of surface pretreatments on the quality of trivalent chromium process coatings on aluminum alloy, Appl. Surf. Sci. 423 (2017) 927–938, doi:10.1016/j.apsusc.2017.06.246.

[54] L. Suo, Y. Hu, H. Li, M. Armand, L. Chen, A new class of solvent-in-salt electrolyte for high-energy rechargeable metallic lithium batteries, Nat. Commun. 4 (2013) 1481, doi:10.1038/ncomms2513.

[55] A.K. Shukla, W.A. Baeslack, Study of microstructural evolution in friction-stir welded thin-sheet Al-Cu-Li alloy using transmission-electron microscopy, Scr. Mater. 56 (2007) 513–516, doi:10.1016/j.scriptamat.2006.11.028.

[56] J.V.S. Araujo, A.F.S. Bugarin, U. Donatus, C.S.C. Machado, F.M. Queiroz, M. Terada, A. Astarita, I. Costa, Thermomechanical treatment and corrosion resistance correlation in the AA2198 Al-Cu-Li alloy, Corros. Eng. Sci. Technol. 54 (2019) 575–586, doi:10.1080/1478422X.2019.1637077.